



available at www.sciencedirect.com



journal homepage: www.elsevier.com/locate/jhydrol



A mathematical model for seepage of deeply buried groundwater under higher pressure and temperature

Tao Huang ^{a,*}, John W. Rudnicki ^{b,1}

^a School of Environmental Science and Engineering, Southwest Jiaotong University, No. 111, North 1st Section, The 2nd Loop Road, Chengdu, Sichuan 610031, PR China

^b Department of Civil and Environmental Engineering, Northwestern University, 2145 Sheridan Road, Evanston, IL 60208-3109, USA

Received 26 August 2004; received in revised form 11 November 2005; accepted 15 November 2005

KEYWORDS

Higher pressure and temperature;
Deeply buried groundwater;
Brine;
Seepage mathematical model

Summary Deeply buried groundwater, such as brine, is an important industrial raw material with high economic value. Because brine frequently exists under higher temperature and pressure, the quantitative prediction of its seepage field is very difficult. Here we study the migration of deeply buried groundwater by using a numerical simulation based on laboratory test results. In particular, we express the pressure and temperature variation of seepage parameters such as hydraulic conductivity K and specific storage coefficient S in terms of the corresponding variation of the solid skeleton's permeability k , porosity n , compressibility coefficient β_s , and seepage fluid's viscosity μ and compressibility coefficient β_w . Then through mathematical transformation and linearization methods, the mathematical model with pressure and temperature dependent coefficients is reduced to the same form as the standard one for seepage flow. The results are successfully applied to the Moxi structure in Sichuan basin. The results show that the effect of higher pressure and temperature should be taken into account for quantitative study of deeply buried groundwater, and that the effects are easily included by the transformation of the mathematical model to standard form.

© 2005 Elsevier B.V. All rights reserved.

Introduction

Compared with groundwater in a shallow layer, deeply buried groundwater lies in a higher pressure and temperature environment. Yang (1990) and Kok et al. (2002) pointed out that these higher pressure and temperature conditions

* Corresponding author. Tel.: +86 28 8760 2461; fax: +86 28 8760 1545.

E-mail addresses: taohuang70@126.com (T. Huang), jwrudn@northwestern.edu (J.W. Rudnicki).

¹ Fax: +1 847 491 4011.

should be included in quantitative research on deeply buried groundwater. In fact, this topic is related to the issue of coupling between seepage and stress in groundwater's migration, and it involves two aspects: the effect of seepage on stress and the effect of stress on seepage. The first has been extensively studied since the 1980s (e.g., Li and Desai, 1983; Borja, 1992; Hsi and Small, 1992; Reid and Iversen, 1992; Fernandez and Alvarez, 1994; Budhu and Gobin, 1995; Fung and Wong, 1996; Jouanna et al., 1998; Zhao et al., 1999; Tomlinson and Vaid, 2000; Sridharan and Prakash, 2001; Simon and Collison, 2001; Liu and Ng, 2003; Corfdir, 2004; Rinaldi et al., 2004). The second aspect has also been an active area of research in geomechanics for many years, especially in the fields of nuclear waste disposal and geothermal extraction, with successful development of numerical modeling and field/lab tests. Some of the very successful FEM codes were presented in Jing et al. (1995) and Rutqvist et al. (2001). Despite this high level of activity, determining the effect of stress on seepage of deeply buried groundwater remains difficult and the simple and convenient methods that are employed to study the migration of shallow groundwater cannot be used.

Normally, deeply buried groundwater occurs in confined aquifers and, in most cases the aquifer's thickness is far less than its horizontal length (the difference can be achieve to tens, hundreds and thousands meters). Therefore, we can assume that water flow is horizontal everywhere in the confined aquifer. Based on this assumption, the governing equation for describing groundwater migration in a confined aquifer and its corresponding boundary and initial conditions are generally as follows (Bear, 1988):

$$\frac{\partial}{\partial x} \left(MK_x \frac{\partial H}{\partial x} \right) + \frac{\partial}{\partial y} \left(MK_y \frac{\partial H}{\partial y} \right) + Q = S \frac{\partial H}{\partial t},$$

$$\left(MK_x \frac{\partial H}{\partial x} \cdot \frac{\partial y}{\partial x} - MK_y \frac{\partial H}{\partial y} \cdot \frac{\partial x}{\partial y} \right)_{\Psi} + \alpha \cdot H|_{\Gamma} = \beta, \quad (1)$$

$$H|_{\Gamma} = H(x, y, t),$$

$$H(x, y, 0) = H_0(x, y),$$

where H is the head of groundwater in the confined aquifer; H_0 is the initial head function of groundwater; M is the thickness of the confined aquifer; K_x and K_y are the principal hydraulic conductivity in the x and y directions, respectively; S is the layer's storage coefficient, given in terms of S_s , the standard specific storage by $S = MS_s$ and Q is the layer's extraction or discharge yield; Ψ and Γ are the portions of the boundary on which the flux and potential are prescribed; and α , β are predetermined parameters, that depend on the flux boundary condition.

This model is often used to simulate the shallow confined groundwater migration, and the results normally agree well with observations. But for deeply buried groundwater such as brine, this model is inadequate (Academic Institute of Hydrogeological and Engineering Geology of Chinese Geological Ministry, 1982). At depths greater than 1000 m, the temperature and pressure are much higher than at shallower depths and, consequently, the characteristics of the seepage fluid and the storage aquifer are sensitive to changes in temperature and pressure. Therefore, the coefficients in Eq. (1) cannot be treated as constant. Because of the variation of the seepage parameters with pressure related to groundwater's potential, existing computer pro-

grams for shallow groundwater flow, based on numerical simulation methods such as the finite element method, cannot be applied successfully to solving this case. Therefore, an open question is how to set up a method not only for characterizing the deeply buried groundwater migration but also to implement it in a way that requires minimal modification of existing numerical simulations.

Some hydrogeologists, such as Yang (1995), have attempted to overcome this difficulty by choosing seepage parameters such as hydraulic conductivity or permeability and specific storage coefficient to reflect higher pressure and temperature conditions. This is, however, not sufficient and it is necessary to include the dependence of the parameters on temperature and pressure. In this paper, we include this temperature and pressure dependence based on laboratory tests. The nature of this dependence is, however, such that, after mathematical transformation, it can be included in standard numerical simulation methods with a little alteration. We note, however, that in this paper we assume that the rock has isotropic permeability and the stress state is hydrostatic. Because deeply buried groundwater often lies in a relatively inactive geological environment, the effects of tectonic stress changes can be neglected and the above assumption can be regarded as reasonable.

Parameter variation under higher pressure and temperature

In hydrogeology, the seepage parameters such as hydraulic conductivity K and specific storage coefficient S can be represented in terms of the solid skeleton's permeability k , porosity n , compressibility coefficient β_s and seepage fluid's density ρ , viscosity μ , compressibility coefficient β_w as follows (Shen, 1985):

$$K = \frac{k\rho g}{\mu}, \quad (2)$$

$$S = M \cdot S_s = M \cdot \rho(n\beta_w + \beta_s). \quad (3)$$

In addition, the solid skeleton's compressibility coefficient β_s can also be expressed in terms of bulk modulus K_b , which is given in terms of Young's modulus E and Poisson's ratio ν , as

$$\beta_s = \frac{1}{K_b} = \frac{3(1 - 2\nu)}{E}. \quad (4)$$

From these three equations we can deduce that study of seepage parameters' variation under higher pressure and temperature is equivalent to study of the variation of a series of parameters such as solid skeleton's permeability k , porosity n , Young's modulus E , Poisson's ratio ν and seepage fluid's density ρ , viscosity μ , and compressibility coefficient β_w .

Solid skeleton's permeability k

Morita and Gray (1992) measured absolute permeability for Berea sandstone under various loading paths at temperatures from 21 to 193 °C. Holder et al. (1993) discussed air and gas permeability variations versus static deformations for dry, brine-saturated, and partially saturated Shaley sandstone

from a fluvial-deltaic depositional environment. Li et al. (1994) reported that there are coupled relations between the stress–strain and permeability parameters of rock based on the compaction test of Yin Zhuang sandstone. Asadi et al. (1997) employed the finite element method to evaluate stress distribution within the sandstone formation as the result of a perforation job, which involved three distinct steps: (1) jet temperature effect; (2) jet pressure effect, and (3) combined jet temperature and pressure effects. At the same time he pointed out that as a result, rock physical structure will change to a lower bulk density than that of unshocked rock, causing a sudden decrease in formation porosity and hence formation permeability. Menendez et al. (2001) applied confocal scanning laser microscopy to investigate the important geological processes including cementation and diagenetic compaction in sandstone and hydrothermal alteration in granular materials. They concluded that the large drop in permeability (six orders of magnitude), when comparing non-altered to altered samples, is due to a complete change of the pore structure and a strong reduction of the mean pore size. Skomedal et al. (2002) performed a laboratory testing program to investigate the behavior of the sandstone of an reservoir when subjected to realistic in situ stresses, pore pressures and stress changes due to production. They found that the Terzaghi effective stress definition was most suitable to handle the different mechanisms. Based on that study the relevant material properties such as mechanical permeability were defined. Kok et al. (2002) carried out a laboratory project to determine reservoir properties like permeability under in situ stress conditions and to observe the effects of axial stresses on reservoir rocks as sandstone, limestone and Berea sandstone. Zeng et al. (2003) conducted a series of laboratory experiments to investigate the influence of overburden and in situ stresses on non-Darcy gas flow behavior in Dakota sandstone. They found that with the increase of overburden and in situ average effective normal stresses, permeability decreases, and in contrast, average shear stress did not appear to influence the permeability. These tests confirm that the effect of variation of temperature and pressure on porous media's permeability is very complicated.

For reasons of feasibility and limited testing capacity, we take sandstone as a typical porous media sample to determine the variation of solid skeleton's permeability responding to different temperature and pressure (effective stress) levels. The samples are purplish red sandstone from Emei. The composition is approximately 70% quartz, 10–15% calcite, and 10% feldspar, iron or calcium bond. Cylindrical samples with 2.5 cm in diameter and 3.5 cm in height were cut from a large sandstone block by the water drilling method.

Among them we took four as test samples that have an initial porosity (determined by helium aid method) ranging from 19.9% to 20.1% and a density ranging from 2.13 to 2.15 g/cm³.

In the tests we adopt Darcy's steady flow method to measure the sample's permeability. That is, the sandstone sample's permeability can be calculated from some measurable parameters such as flow through the sample, seepage pressure difference and so on. The corresponding calculation equation is identified as

$$k = \frac{q\mu L}{A\Delta p} \times 10^{-1}, \quad (5)$$

where k is the sample's permeability (μm^2); q is the flow yield through the sample (ml/s); μ is fluid viscosity (MPa s); L is denoted as the sample's length (cm); and Δp is seepage pressure difference between the top and bottom sides of the sample (MPa); A , the sample's cross-section area (cm^2), is given by

$$A = \pi d^2 / 4, \quad (6)$$

where d is the diameter of the sample (cm).

We used a rock core flow instrument known as LDY-III, which is manufactured by Hai'an Petroleum Instrument Co. in Jiangsu, China. Its primary properties are listed as follows: (i) test temperature ranges from indoor temperature to 150 °C, and has the error of ± 5 °C; (ii) confining pressure is listed from 0 to 40 MPa, and corresponding error is ± 0.001 MPa. Before the test we subjected the samples to a vacuum for 3.5 h, then submerged them in distilled water for two days. This procedure guarantees single-phase flow in samples during the test process. The first step in the test process is putting the sample in the rock core holder, which lies in a constant temperature box, and heating the box to a pre-set level. Then we hold the temperature fixed for 1.5 h. The second step is exerting confining pressure to a preset level through manual pumping and holding it fixed for half an hour. The following step is to induce seepage in the rock sample by exerting seepage pressure on the sample by establishing horizontal flow by pumping on the entry side and keeping in touch with the atmosphere on the exit side. Then we record the steady flow yield through the sample under this confined pressure. We repeat the test procedure from step 2, and measure the corresponding steady flow yield through the sample under seven different confining pressure levels. We repeat this test procedure on other samples under different temperature levels and get the corresponding results.

Finally, according to Eq. (5) we can calculate the corresponding sample's permeability under the different temperatures and confining pressures. The results are displayed in Table 1.

Table 1 The permeability values of sandstone under different temperature and confined pressure

Rock sample number	Temperature T (°C)	k ($\times 10^{-3} \mu\text{m}^2$)						
		$\sigma' = 1$ MPa	$\sigma' = 3$ MPa	$\sigma' = 5$ MPa	$\sigma' = 7$ MPa	$\sigma' = 10$ MPa	$\sigma' = 15$ MPa	$\sigma' = 25$ MPa
1	20	9.73	5.28	4.62	4.30	4.24	4.05	3.65
2	30	5.16	4.76	4.28	3.95	3.53	3.11	2.65
3	40	4.87	4.18	3.96	3.73	3.30	3.06	2.62
4	60	2.35	2.10	1.97	1.90	1.77	1.61	1.39

Figs. 1 and 2 show the samples' permeability variation versus pressure and temperature. As shown in Fig. 1, the permeability decreases with increasing confining pressure for a fixed temperature. This decrease can be expressed in terms of a negative exponential function:

$$k = a_k k_0 e^{-b_k(\sigma' - p_0)}, \quad (7)$$

where a_k and b_k are simulation constants; and σ' is confining pressure; k_0 is the initial permeability when the pressure is p_0 , which is normally taken as the value of 1 standard atmosphere pressure.

Fig. 1 also shows that curves of k versus σ' tend to become flat with increasing temperature, indicating that the increase of temperature diminishes the effect of pressure on sample's permeability. Fig. 2 demonstrates that sandstone's permeability decreases with increasing temperature at fixed confining pressure, and confirms that increasing pressure reduces the permeability. This behavior indicates that the increasing pressure dominates the effect of temperature on sandstone's permeability. These two characteristics shown in Figs. 1 and 2 can be attributed to two physical processes. On the one hand, the solid skeleton of the sandstone undergoes thermal expansion with increasing temperature. Thus the seepage passageways between pores are compressed, and consequently, the sandstone's permeability decreases with increasing temperature. On the other hand, increasing pressure causes the compressibility of pores to decrease and flow passages to become more and more restricted. As a result, the compressive effect of pressure and thermal expansion on pores is diminished.

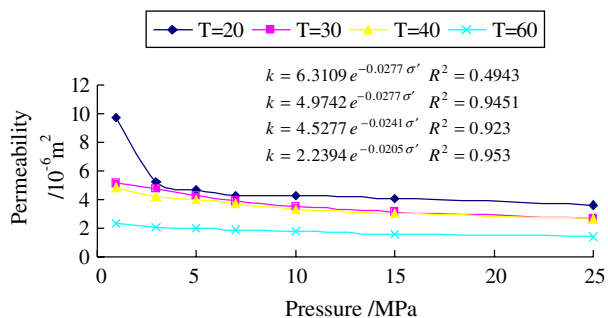


Figure 1 Sandstone's permeability versus pressure under different temperature levels.

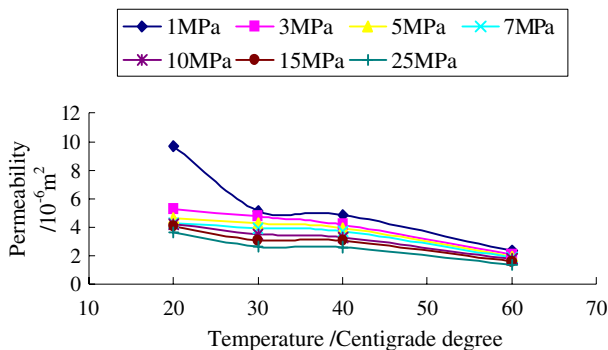


Figure 2 Sandstone's permeability versus temperature under different pressure levels.

Solid skeleton's porosity n

Porosity is a parameter used to represent the volumetric amount of pores or cracks in rock. Many scientists (e.g., Palciauskas and Domenico, 1982; Hart and John, 1986; Rutter and Hadizadeh, 1991; Asadi et al., 1997; Lander and Walderhaug, 1999; Khaksar et al., 1999; Asadi et al., 2001; Ehlig-Economides and Economides, 2002; Kok et al., 2002; Lindborg, 2002; Fisher et al., 2003; Chardac et al., 2003) have carried out theoretical studies that involved the effects of temperature and pressure on rock porosity and its application to coupling among temperature, seepage, and stress.

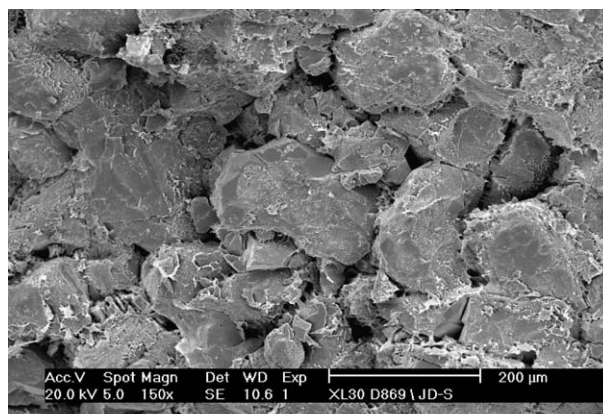
If the compressibility of solid grains is neglected (compared to void compressibility), then the compressibility of rock at a fixed temperature and pressure is equal to the compressibility of porosity. The porosity can be calculated from Eq. 8 using the measured pore volume of rock sample at fixed pressure and temperature

$$n = \frac{V_p}{V_s + V_p} \times 100\%, \quad (8)$$

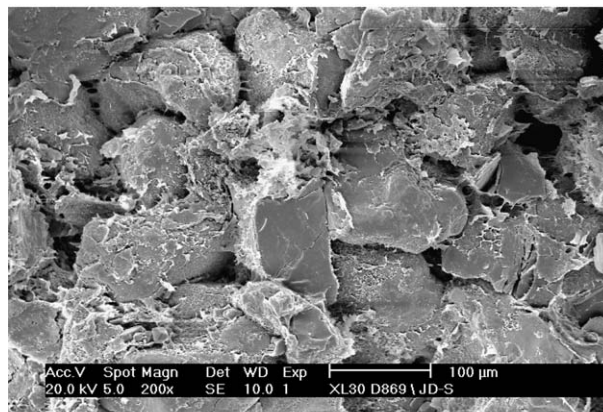
where n is porosity (%); V_p is the pore volume (cm^3); and V_s is the solid volume (cm^3).

In this test we use the same sandstone samples as in the permeability test, and their SEM images are shown in Fig. 3.

The tests are conducted using the Rock Compressibility System 3006, which is manufactured by TEMCO Inc. With



(a) 150X



(b) 200X

Figure 3 SEM images of sandstone's sample.

this system, the confining pressure can be as high as 70 MPa and corresponding minimum pressure recognition ratio is 1 psi (1 psi \approx 0.006897 MPa).

The test procedure is scheduled as follows: Firstly, turn on the Rock Compressibility System instrument and preheat it for about half an hour. Then wrap the sandstone sample with specially made thermal plastic cover, and put it into the rock core holder. Afterwards, with a 1.38 MPa pressure level, the sample is sealed, and we can keep the rock core and its corresponding inner pressure system vacuum over 8 h. Then saturate the rock core and inner pressure system with salt water adequately, and increase the confining pressure to 2.76 MPa and inner pressure to 1.38 MPa. According to test rules, during test we can heat the constant temperature box, in which the rock core holder lies, to a preset level with the heating system, and check this temperature level immediately with the temperature control system. When the pore pressure in the rock core becomes steady, the values of pore pressure and volumetric pump can be recorded as the reference value for the test. Then exert confining pressure through the pressure adding system, and adjust the pore pressure to the above-mentioned reference

value after confined pressure and pore pressure achieve steady state at this level. Therefore, when the confining pressure becomes steady by adjusting the pore pressure to the reference value, we can record the confining pressure level value and the corresponding variation of pore volume, which is equal to the volume of salt water squeezed out from the sample. Through this variation of pore volume, rock sample's initial porosity (Table 2), and total volume, we can calculate the relevant porosity by Eq. (8). Then repeat the above procedure to test the sample on other confined pressure and preset temperature levels. It should be mentioned that the reference value of pore pressure must be kept constant during the same temperature level test, and the criterion of achieving steady state pressure is that the figure-displayed pressure value in the instrument fluctuates less than 1 psi in one minute.

The test results are shown in Table 2, and the corresponding curves are drawn in Fig. 4.

From Fig. 4 we can see that at a fixed temperature level, the sample's porosity decreases with each increment of effective pressure. The decrease is more abrupt at lower effective pressures and diminishes with increasing effective

Table 2 Values of sandstone's porosity under different temperature and effective pressure

Sample 1	Temperature T ($^{\circ}\text{C}$)	22.6	Pore pressure (MPa)	1.274	Initial porosity n_0 (%)	19.9			
Effective pressure = confined pressure – pore pressure (MPa)	0.896	2.995	4.997	8.926	12.773	19.562	27.379	33.729	47.228
Porosity n (%)	19.73	19.32	19.04	18.59	18.44	18.17	17.83	17.66	17.28
Sample 2	Temperature T ($^{\circ}\text{C}$)	30.0	Pore pressure (MPa)	1.354	Initial porosity n_0 (%)	20.0			
Effective pressure = confined pressure – pore pressure (MPa)	1.248	3.101	5.379	9.348	13.845	21.457	29.613	40.438	
Porosity n (%)	19.84	19.48	19.09	18.59	18.24	17.82	17.48	17.13	
Sample 3	Temperature T ($^{\circ}\text{C}$)	34.0	Pore pressure (MPa)	1.868	Initial porosity n_0 (%)	19.9			
Effective pressure = confined pressure – pore pressure (MPa)	1.871	3.860	6.711	10.910	15.381	2.066	30.023	36.243	46.537
Porosity n (%)	19.70	19.29	18.86	18.41	18.10	17.79	17.50	17.31	17.04
Sample 4	Temperature T ($^{\circ}\text{C}$)	40.0	Pore pressure (MPa)	8.045	Initial porosity n_0 (%)	20.0			
Effective pressure = confined pressure – pore pressure (MPa)	1.721	3.927	6.536	9.325	14.005	20.864	28.291	35.999	45.212
Porosity n (%)	19.90	19.39	19.00	18.66	18.27	17.88	17.58	17.27	17.03
Sample 5	Temperature T ($^{\circ}\text{C}$)	50.0	Pore pressure (MPa)	8.893	Initial porosity n_0 (%)	19.9			
Effective pressure = confined pressure – pore pressure (MPa)	2.568	4.875	8.260	12.621	17.684	24.055	30.973	37.745	45.369
Porosity n (%)	19.76	19.00	18.94	18.59	18.31	18.05	17.82	17.59	17.41
Sample 6	Temperature T ($^{\circ}\text{C}$)	60.0	Pore pressure (MPa)	11.538	Initial porosity n_0 (%)	19.9			
Effective pressure = confined pressure – pore pressure (MPa)	7.192	11.611	15.517	20.458	26.647	33.310	40.437	47.824	
Porosity n (%)	19.22	18.94	18.75	18.55	18.33	18.09	17.93	17.74	

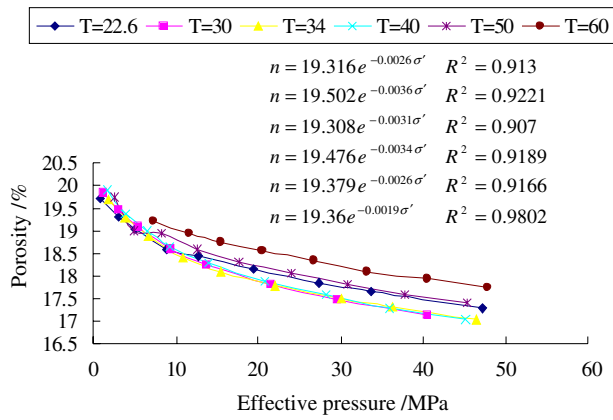


Figure 4 Sandstone's porosity versus effective pressure under different temperature levels.

pressure. This behavior is the result of two effects: initially, the pore volume decreases much more due to the effective compressibility of the pores. On the other hand, because the void space that can be compressed is limited, the pore's compressibility coefficient C_p (defined as $C_p = -(1/V_p)(dV_p/d\sigma')$, where σ' is effective pressure and V_p is mentioned in Eq. (8)) will decrease rapidly with the increasing of effective pressure.

Through curve fitting, the decrease of porosity with effective pressure, which is shown in Fig. 4, can be expressed in terms of the negative exponential function:

$$n = a_n n_0 e^{-b_n(\sigma' - p_0)}, \quad (9)$$

where a_n and b_n are simulation constants; and σ' is confined pressure; n_0 is the initial permeability when the pressure is p_0 , which is normally taken as 1 standard atmosphere pressure.

At the same time, it seems pretty clear from Fig. 4 that there is not much difference between the curves at different temperatures. This phenomenon demonstrates that the porosity does not vary much with temperature (in the measured range) and, hence, the dependence of porosity on temperature can be neglected.

Solid skeleton's compressibility coefficient β_s

As mentioned above, the solid skeleton's compressibility coefficient, β_s , is also expressed in terms of bulk modulus K_b , which can be presented in terms of Young's modulus E and Poisson's ratio ν , as

$$\beta_s = \frac{1}{K_b} = \frac{3(1-2\nu)}{E}. \quad (4)$$

Therefore, the variation of solid skeleton's compressibility coefficient β_s under higher pressure and temperature is

equivalent to variation of solid skeleton's Young's modulus E and Poisson's ratio ν .

Theoretical and practical studies have shown that the small temperature change has little effect on the rock's Young's modulus, E and Poisson's ratio, ν (Yang, 1995). So here we ignore the effect of temperature variation on sandstone's Young's modulus and Poisson's ratio.

In an additional test we measure the sandstone's Young's modulus and Poisson's ratio under different pressure levels, and calculate the corresponding sandstone's compressibility coefficient β_s by Eq. (4). The resulting values are shown in Table 3 and plotted in Fig. 5.

We also find that the decrease of sandstone's compressibility coefficient, β_s , with pressure can be described in terms of the negative exponential function (Eq. (10))

$$\beta_s = a_{\beta_s} \beta_{s0} e^{-b_{\beta_s}(\sigma' - p_0)}, \quad (10)$$

where a_{β_s} , b_{β_s} are simulation constants; and σ' is confining pressure; β_{s0} is the initial compressibility coefficient when pressure is p_0 , which is normally taken the value of 1 standard atmosphere pressure.

Seepage fluid's density ρ

Here we take the brine as an example of deeply buried groundwater and make a series of tests on it. As the byproduct of natural gas, brine normally is generated through long geological history and is buried in deep storage structures. Therefore, it has higher mineral concentration than normal groundwater and salt can be extracted as a resource. The tests summarized in Table 4 show that the density changed only 3.1% when temperature increases from 0 to 95.0 °C. Because the effect of temperature variation on brine's density is so weak, we can neglect it in this research.

Seepage fluid's viscosity μ

In contrast to the brine's density, the viscosity varied strongly with temperature. At the same time, the effect of pressure change on brine's viscosity is so weak that it can be ignored here. Table 5 tabulates the relevant results.

The brine's viscosity decreases with increasing temperature, as shown in Fig. 6, and can also be described with a negative exponential function

$$\nu = a_\nu \nu_0 e^{-b_\nu(T - T_0)}, \quad (11)$$

where a_ν , b_ν are simulation constants; and T is temperature; ν_0 is the initial viscosity when temperature value is T_0 .

Seepage fluid's compressibility coefficient β_w

As with the solid skeleton's compressibility coefficient, β_s , the brine's compressibility coefficient, β_w , expresses the

Table 3 Values of E , ν and β_s under different effective pressure

Effective pressure (MPa)	0	2	4	8	12	16	20	30	40	50
Young's modulus E (GPa)	25.67	26.34	26.82	27.80	28.82	29.88	30.97	33.89	37.08	40.57
Poisson's ratio ν	0.125	0.126	0.128	0.131	0.134	0.137	0.140	0.149	0.158	0.167
Compressibility coefficient β_s (1/GPa)	0.217	0.213	0.208	0.199	0.191	0.182	0.174	0.155	0.138	0.123

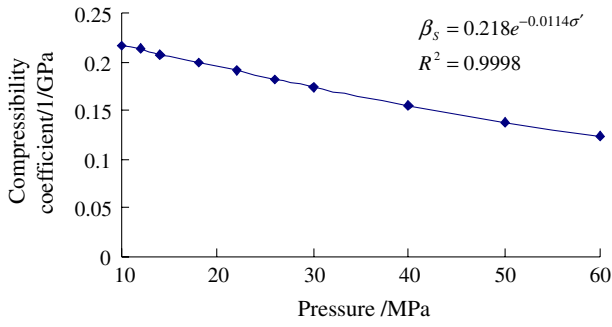


Figure 5 Sandstone's compressibility coefficient versus pressure.

volumetric variation amount responding to unit pressure change. Here we conduct a series of tests that show the effect of pore pressure change on brine's compressibility coefficient at two different temperature levels. Table 6 and Fig. 7 show the relevant results.

The relationship between brine's compressibility coefficient, β_w , and pore pressure from Table 6 can also be expressed in terms of the same negative exponential function

$$\beta_w = a_{\beta_w} \beta_{w0} e^{-b_{\beta_w}(p-p_0)}, \quad (12)$$

where a_{β_w} , b_{β_w} are simulation constants; and p is pore pressure; β_{w0} is the initial compressibility coefficient when the pore pressure is p_0 , which is normally taken as 1 standard atmosphere pressure.

Mathematical model for migration of deeply buried groundwater

As discussed above, the seepage parameters of deeply buried groundwater such as hydraulic conductivity, K , and storage coefficient, S , can be expressed as functions of temperature and pressure by means of parameters such as solid skeleton's permeability k , porosity n , compressibility coefficient β_s , and seepage fluid's density ρ , viscosity μ , and compressibility coefficient β_w .

Here we take deeply buried brine as an example and set up its mathematical model under higher pressure and temperature. As is well known, the overburden weight is carried by both brine and solid skeleton. The part carried by brine is the pore pressure p , and another part carried by the solid skeleton is called effective stress σ' (Huang, 1996). For an overburden weight P , the effective stress is

$$\sigma' = P - p. \quad (13)$$

Table 4 Values of brine's density ρ under different temperature

Temperature T (°C)	0	4.0	18.5	46.0	54.5	73.0	95.0
Brine's density ρ (g/cm ³)	1.1724	1.1705	1.1689	1.1638	1.1557	1.1437	1.1361

Table 5 Values of brine's viscosity μ under different temperature

Temperature T (°C)	0	4.0	18.5	46.0	54.5	73.0	95.0
Brine's viscosity μ (P)	1.9867	1.7238	1.3081	0.7417	0.6689	0.4810	0.3624

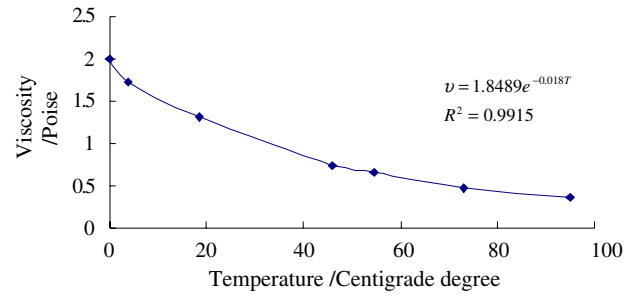


Figure 6 Brine's viscosity versus different temperature levels.

By using (13), Eqs. (7), (9) and (10) can be expressed in terms of the pore pressure p .

$$k = a_k k_0 e^{b_k(p-p_0)}, \quad (14)$$

$$n = a_n n_0 e^{b_n(p-p_0)}, \quad (15)$$

$$\beta_s = a_{\beta_s} \beta_{s0} e^{b_{\beta_s}(p-p_0)}. \quad (16)$$

In addition, Eqs. (11) and (12) express the dependence of the brine behavior on pressure and temperature.

Substituting Eqs. (2) and (3) into Eq. (1) yields

$$\begin{aligned} \frac{\partial}{\partial x} \left(M \frac{k_x \rho g}{v} \frac{\partial H}{\partial x} \right) + \frac{\partial}{\partial y} \left(M \frac{k_y \rho g}{v} \frac{\partial H}{\partial y} \right) + Q \\ = M \rho (n \beta_w + \beta_s) \frac{\partial H}{\partial t}. \end{aligned} \quad (17)$$

Expressing the head H in terms of the pore pressure

$$p = \rho g H \quad (18)$$

then gives

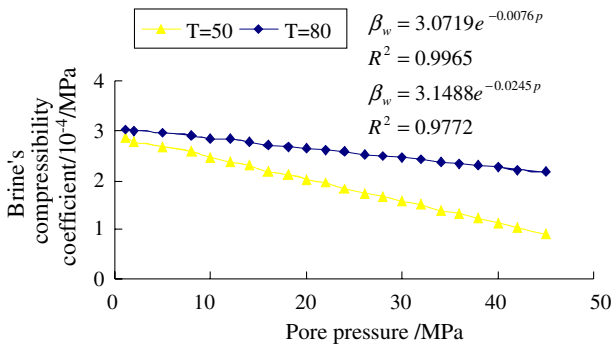
$$\frac{\partial}{\partial x} \left(M \frac{k_x}{v} \frac{\partial p}{\partial x} \right) + \frac{\partial}{\partial y} \left(M \frac{k_y}{v} \frac{\partial p}{\partial y} \right) + Q = \frac{M}{g} (n \beta_w + \beta_s) \frac{\partial p}{\partial t}. \quad (19)$$

Substituting the parameter's variation functions (Eqs. (11)–(16)) into Eq. (19) gives

$$\begin{aligned} \frac{\partial}{\partial x} \left(M \frac{\alpha_k k_{0x}}{\alpha_v v_0 e^{-b_v(T-T_0)} e^{b_k(P-p_0)}} e^{b_{kp}} \frac{\partial p}{\partial x} \right) \\ + \frac{\partial}{\partial y} \left(M \frac{\alpha_k k_{0y}}{\alpha_v v_0 e^{-b_v(T-T_0)} e^{b_k(P-p_0)}} e^{b_{kp}} \frac{\partial p}{\partial y} \right) + Q \\ = \frac{M}{g} \left(\frac{\alpha_n n_0 \alpha_{\beta_w} \beta_{w0} e^{b_{\beta_w} p_0}}{e^{b_n(P-p_0)}} e^{(b_n - b_{\beta_w})p} + \frac{\alpha_{\beta_s} \beta_{s0}}{e^{b_{\beta_s}(P-p_0)}} e^{b_{\beta_s} p} \right) \frac{\partial p}{\partial t}. \end{aligned} \quad (20)$$

Table 6 Values of brine's compressibility coefficient β_w under different pore pressure and temperature

Pore pressure (MPa)	1	2	5	8	10	12	14	16	18	20	22
Brine's compressibility coefficient β_{w1} ($T = 50^\circ\text{C}$) ($\times 10^{-4}$ MPa)	2.565	2.756	2.683	2.575	2.457	2.348	2.293	2.184	2.101	2.019	1.938
Brine's compressibility coefficient β_{w2} ($T = 80^\circ\text{C}$) ($\times 10^{-4}$ MPa)	3.032	2.978	2.962	2.892	2.849	2.824	2.770	2.718	2.692	2.639	2.614
β_{w2}/β_{w1}	1.182	1.081	1.104	1.123	1.151	1.203	1.208	1.245	1.281	1.307	1.349
Pore pressure (MPa)	24	26	28	30	32	34	36	38	40	42	45
Brine's compressibility coefficient β_{w1} ($T = 50^\circ\text{C}$) ($\times 10^{-4}$ MPa)	1.827	1.745	1.663	1.580	1.497	1.387	1.331	1.221	1.138	1.055	0.926
Brine's compressibility coefficient β_{w2} ($T = 80^\circ\text{C}$) ($\times 10^{-4}$ MPa)	2.588	2.534	2.481	2.455	2.429	2.376	2.322	2.296	2.270	2.216	2.171
β_{w2}/β_{w1}	1.417	1.452	1.492	1.554	1.623	1.713	1.745	1.880	1.995	2.100	2.344

**Figure 7** Brine's compressibility coefficient versus pore pressure under different temperature levels.

Making the substitution $u = e^{b_k p}$ makes it possible to write certain exponential terms as

$$e^{(b_n - b_{\beta_w})p} = e^{\frac{(b_n - b_{\beta_w})p}{b_k}} = e^{b_k p \frac{b_n - b_{\beta_w}}{b_k}} = u^{\frac{b_n - b_{\beta_w}}{b_k}}, \quad (21)$$

$$e^{b_{\beta_s} p} = e^{\frac{b_{\beta_s} p}{b_k}} = e^{b_k p \frac{b_{\beta_s}}{b_k}} = u^{\frac{b_{\beta_s}}{b_k}} \quad (22)$$

and, when combined with derivatives of the pore pressure in (20), they become

$$e^{b_k p} \frac{\partial p}{\partial x} = u \frac{\partial p}{\partial x} = \frac{1}{b_k} \frac{\partial u}{\partial x}, \quad (23)$$

$$e^{b_k p} \frac{\partial p}{\partial y} = u \frac{\partial p}{\partial y} = \frac{1}{b_k} \frac{\partial u}{\partial y}, \quad (24)$$

$$e^{(b_n - b_{\beta_w})p} \frac{\partial p}{\partial t} = u^{\frac{b_n - b_{\beta_w}}{b_k}} \frac{\partial p}{\partial t} = \frac{1}{b_k} u^{\frac{b_n - b_{\beta_w}}{b_k} - 1} \frac{\partial u}{\partial t}, \quad (25)$$

$$e^{b_{\beta_s} p} \frac{\partial p}{\partial t} = u^{\frac{b_{\beta_s}}{b_k}} \frac{\partial p}{\partial t} = \frac{1}{b_k} u^{\frac{b_{\beta_s}}{b_k} - 1} \frac{\partial u}{\partial t}. \quad (26)$$

Therefore, Eq. (20) can be rewritten as

$$\begin{aligned} & \frac{\partial}{\partial x} \left(M \frac{\alpha_k k_{0x}}{\alpha_v \nu_0 e^{-b_v(T-T_0)} e^{b_k(P-P_0)}} \frac{\partial u}{\partial x} \right) \\ & + \frac{\partial}{\partial y} \left(M \frac{\alpha_k k_{0y}}{\alpha_v \nu_0 e^{-b_v(T-T_0)} e^{b_k(P-P_0)}} \frac{\partial u}{\partial y} \right) + Q b_k \\ & = \frac{M}{g} \left(\frac{\alpha_n n_0 \alpha_{\beta_w} \beta_{w0} e^{b_{\beta_w} P_0}}{e^{b_n(P-P_0)}} u^{\frac{b_n - b_{\beta_w}}{b_k} - 1} + \frac{\alpha_{\beta_s} \beta_{s0}}{e^{b_{\beta_s}(P-P_0)}} u^{\frac{b_{\beta_s}}{b_k} - 1} \right) \frac{\partial u}{\partial t}. \end{aligned} \quad (27)$$

Because the main effect of the variation of pressure is already included in u , Ge (1982) has suggested that the non-linear terms in u on the right side can be linearized about the condition of normal pressure $p = p_0 = 1 \text{ atm} = 0.1 \text{ MPa}$. In addition, the magnitude of parameters b_k is in the range of $10^{-2} - 10^{-4}$. Because the product of $b_k p_0$ is relatively small, it can be regarded as approaching zero and therefore $u|_{p=p_0} = e^{b_k p}|_{p=p_0} \approx 1$. Based on these simplifications, we can approximate $u^{\frac{b_n - b_{\beta_w}}{b_k} - 1}|_{p=p_0} \approx 1$ and $u^{\frac{b_{\beta_s}}{b_k} - 1}|_{p=p_0} \approx 1$.

Eq. (27) then becomes

$$\begin{aligned} & \frac{\partial}{\partial x} \left(M \frac{\alpha_k k_{0x}}{\alpha_v \nu_0 e^{-b_v(T-T_0)} e^{b_k(P-P_0)}} \frac{\partial u}{\partial x} \right) \\ & + \frac{\partial}{\partial y} \left(M \frac{\alpha_k k_{0y}}{\alpha_v \nu_0 e^{-b_v(T-T_0)} e^{b_k(P-P_0)}} \frac{\partial u}{\partial y} \right) + Q b_k \\ & = \frac{M}{g} \left(\frac{\alpha_n n_0 \alpha_{\beta_w} \beta_{w0} e^{b_{\beta_w} P_0}}{e^{b_n(P-P_0)}} + \frac{\alpha_{\beta_s} \beta_{s0}}{e^{b_{\beta_s}(P-P_0)}} \right) \frac{\partial u}{\partial t}. \end{aligned} \quad (28)$$

Eq. (28) can be written as

$$\frac{\partial}{\partial x} \left(M K_x^* \frac{\partial u}{\partial x} \right) + \frac{\partial}{\partial y} \left(M K_y^* \frac{\partial u}{\partial y} \right) + Q^* = S^* \frac{\partial u}{\partial t} \quad (29)$$

by defining the following parameters

$$K_x^* = \frac{\alpha_k k_{0x}}{\alpha_v \nu_0 e^{-b_v(T-T_0)} e^{b_k(P-P_0)}}, \quad K_y^* = \frac{\alpha_k k_{0y}}{\alpha_v \nu_0 e^{-b_v(T-T_0)} e^{b_k(P-P_0)}},$$

$$Q^* = Q b_k, \quad S^* = \frac{M}{g} \left(\frac{\alpha_n n_0 \alpha_{\beta_w} \beta_{w0} e^{b_{\beta_w} P_0}}{e^{b_n(P-P_0)}} + \frac{\alpha_{\beta_s} \beta_{s0}}{e^{b_{\beta_s}(P-P_0)}} \right).$$

By replacing H with $u = e^{b_k \rho g H}$ in the boundary and initial conditions in Eq. (1), the transformed model becomes

$$\begin{aligned} & \frac{\partial}{\partial x} \left(M K_x^* \frac{\partial u}{\partial x} \right) + \frac{\partial}{\partial y} \left(M K_y^* \frac{\partial u}{\partial y} \right) + Q^* = S^* \frac{\partial u}{\partial t}, \\ & \left(M K_x^* \frac{\partial u}{\partial x} \cdot \frac{\partial y}{\partial x} - M K_y^* \frac{\partial u}{\partial y} \cdot \frac{\partial x}{\partial y} \right)_{\psi} + \alpha^* \cdot \ln u|_{\psi} = \beta^*, \end{aligned} \quad (30)$$

$$u|_r = u(x, y, t),$$

$$u(x, y, 0) = u_0(x, y),$$

where $\alpha^* = \alpha / \rho g$; $\beta^* = b_k \beta$.

We notice that the new model (Eq. (30)) has the same form as the old model (Eq. (1)). In this new form, the function variable u includes the effects of the pressure variation. In addition, the relative parameters have been

revised to include the variations due to the higher pressure and temperature conditions. Finally, because the new model has the same form as the old, the same numerical programs can be used for the solution.

Applied example

In order to test and verify the suitability and reasonableness of this new model for deeply buried groundwater migration, we choose the brine that lies in the T_{2l}^1 reservoir of the Moxi structure in Sichuan basin as an example, and simulate its distribution.

Some common characteristics for models of brine reservoirs that we adopt here are the following:

1. The brine reservoir is inhomogeneous and anisotropic.
2. The boundary of brine reservoir is impermeable.
3. The brine has higher horizontal piezometric head.
4. There is no obvious change in horizontal direction for the layer of brine reservoir in the same brine reservoir structure. In the vertical direction there is no leakage between the different layers of the brine reservoir.
5. There are numerous wells operating simultaneously in the brine reservoir and, there is interference among these wells.
6. The exploitation yield for every well may be different.
7. The exploitation yield for a well may change with the time.

According to the basic geological and hydrogeological investigation and analysis (Huang, 1996), the reservoir of deeply buried brine lies within the sandstone belonging to Trias. The reservoir is confined and the burial depth is more than 2685 m. The confined water head can reach as high as 5514.83 m. This reservoir also has an average thickness of 65.47 m. Because the angles of deviation from horizontal for both wings of the anticline are relatively small (only 3–5°) and the buried depth of reservoir is far more than its thickness, we model the reservoir as a planar structure. Based on qualitative and quantitative analysis on the brine's distribution, the research area can be divided into three parts such as abundant water part I, moderate abundant water part II, and poor water part III, which are shown in Fig. 8. This figure shows the distribution plan for the brine reservoir T_{2l}^1 in the Moxi structure and, Fig. 9 gives the element mesh for FEM calculation.

In the research area there are 13 wells (shown in Fig. 8) that have variable discharge and pumping rates from February 1991 to May 1993. Therefore, the seepage field of this T_{2l}^1 reservoir can be expressed by the following model:

$$\begin{aligned} \frac{\partial}{\partial x} \left(MK_x^* \frac{\partial u}{\partial x} \right) + \frac{\partial}{\partial y} \left(MK_y^* \frac{\partial u}{\partial y} \right) + Q^* &= S^* \frac{\partial u}{\partial t}, \\ \left(MK_x^* \frac{\partial u}{\partial x} \cdot \frac{\partial y}{\partial x} - MK_y^* \frac{\partial u}{\partial y} \cdot \frac{\partial x}{\partial y} \right)_{\psi} &= 0, \\ u(x, y, 0) &= u_0(x, y), \end{aligned} \quad (31)$$

where ψ is the impermeable boundary; other symbols are the same as before.

For this model's calculation we use the finite element method (FEM) (Xue and Xie, 1980) and, in particular, the program FEMPL007.for (Chen, 1993), which is written in

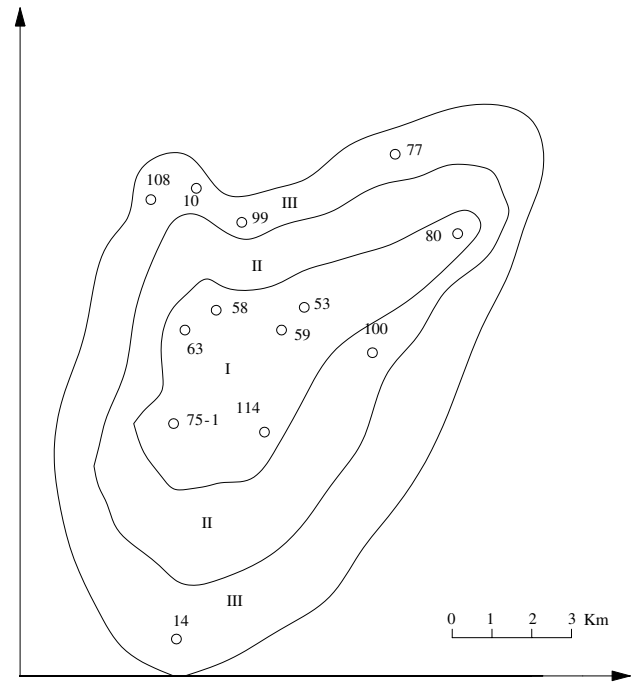


Figure 8 Regional partition plan and well distribution for the brine reservoir T_{2l}^1 in Moxi structure.

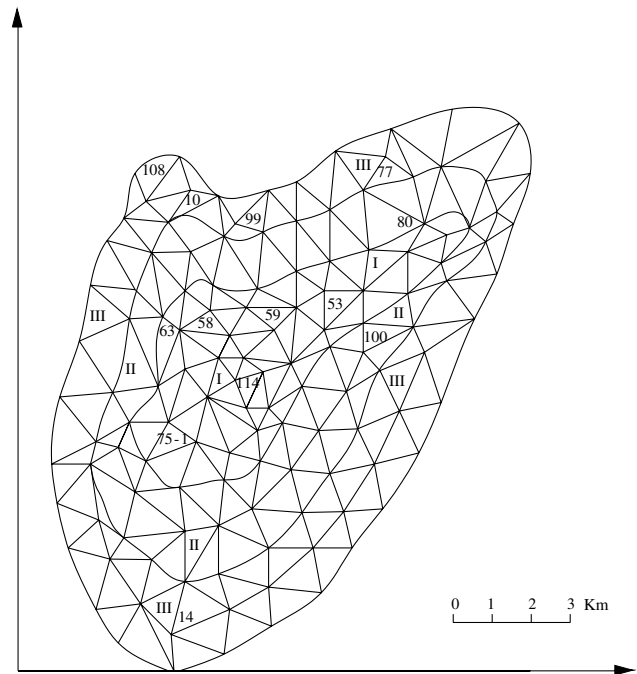


Figure 9 Elements division in FEM calculation for the brine reservoir T_{2l}^1 in Moxi structure.

FORTRAN77 language. The principles for this FEM code can be described as follows:

1. The solution of (31) is equivalent to the problem of minimizing the following function $E(u)$:

$$E(u) = \int \int_D \left\{ \frac{1}{2} \left[MK_x^* \left(\frac{\partial u}{\partial x} \right)^2 + MK_y^* \left(\frac{\partial u}{\partial y} \right)^2 + u \left(S^* \frac{\partial u}{\partial t} - q^* \right) \right] \right\} dx dy. \quad (32)$$

2. The whole research area D can be divided into triangular finite elements. The three nodes for each triangle element are labeled as i, j, k , and the corresponding coordinates are defined as (x_i, y_i) , (x_j, y_j) and (x_k, y_k) . So the values of the function variable u in Eq. (31) are defined as u_i, u_j, u_k at each node of the triangular element. In the interior of each element, the variation of function variable u can be approximated linearly in the form

$$\bar{u}(x, y, t) = N_i u_i + N_j u_j + N_k u_k, \quad (33)$$

where

$$N_i = \frac{1}{2\Delta} \begin{vmatrix} 1 & x & y \\ 1 & x_j & y_j \\ 1 & x_k & y_k \end{vmatrix}, \quad N_j = \frac{1}{2\Delta} \begin{vmatrix} 1 & x & y \\ 1 & x_i & y_i \\ 1 & x_k & y_k \end{vmatrix},$$

$$N_k = \frac{1}{2\Delta} \begin{vmatrix} 1 & x & y \\ 1 & x_i & y_i \\ 1 & x_j & y_j \end{vmatrix}, \quad \Delta = \frac{1}{2} \begin{vmatrix} 1 & x_i & y_i \\ 1 & x_j & y_j \\ 1 & x_k & y_k \end{vmatrix}.$$

3. The function $E(u)$ in the entire domain D is then given as the sum of values of the function in each triangular element:

$$E(u) = \sum_{e \in D} \int \int_e \left\{ \frac{1}{2} \left[MK_x^* \left(\frac{\partial u}{\partial x} \right)^2 + MK_y^* \left(\frac{\partial u}{\partial y} \right)^2 + u \left(S^* \frac{\partial u}{\partial t} - q^* \right) \right] \right\} dx dy = \sum_{e \in D} E^e(u). \quad (34)$$

4. Substituting \bar{u} into Eq. (33) for $E^e(u)$ then gives

$$E^e(\bar{u}) = \int \int_e \left\{ \frac{1}{2} \left[MK_x^* \left(\frac{b_i u_i + b_j u_j + b_k u_k}{2\Delta} \right)^2 + MK_y^* \left(\frac{c_i u_i + c_j u_j + c_k u_k}{2\Delta} \right)^2 + (N_i u_i + N_j u_j + N_k u_k) \cdot \left[S^* \left(N_i \frac{\partial u_i}{\partial t} + N_j \frac{\partial u_j}{\partial t} + N_k \frac{\partial u_k}{\partial t} \right) - q^* \right] \right] \right\} dx dy, \quad (35)$$

where

$$b_i = y_j - y_k, \quad c_i = x_k - x_j,$$

$$b_j = y_k - y_i, \quad c_j = x_i - x_k,$$

$$b_k = y_i - y_j, \quad c_k = x_j - x_i.$$

5. In order to calculate the extremum of the function $E(u)$, we calculate the derivatives of the function $E(u)$ with respect to an arbitrary nodal value:

$$\frac{\partial E(u)}{\partial u_i} = \sum_{e \in D} \frac{\partial E^e(u)}{\partial u_i} \approx \sum_{e \in D} \frac{\partial E^e(\bar{u})}{\partial u_i} = \sum_{e \in D} \{ [A]^e \{u\}^e + [P]^e \{u'\}^e - \{q^*\}^e \}, \quad (36)$$

where

$$[A]^e = \frac{1}{4\Delta} MK_x^* \begin{bmatrix} b_i \\ b_j \\ b_k \end{bmatrix} \cdot \begin{bmatrix} b_i \\ b_j \\ b_k \end{bmatrix}^T + \frac{1}{4\Delta} MK_y^* \begin{bmatrix} c_i \\ c_j \\ c_k \end{bmatrix} \cdot \begin{bmatrix} c_i \\ c_j \\ c_k \end{bmatrix}^T,$$

$$\{u\}^e = \begin{Bmatrix} u_i \\ u_j \\ u_k \end{Bmatrix}, \quad [P]^e = \frac{S^* \Delta}{12} \begin{bmatrix} 2 & 1 & 1 \\ 1 & 2 & 1 \\ 1 & 1 & 2 \end{bmatrix},$$

$$\{u'\}^e = \begin{Bmatrix} \frac{\partial u_i}{\partial t} \\ \frac{\partial u_j}{\partial t} \\ \frac{\partial u_k}{\partial t} \end{Bmatrix}, \quad \{q^*\}^e = \frac{q^* \Delta}{3} \begin{Bmatrix} 1 \\ 1 \\ 1 \end{Bmatrix}.$$

6. Discretization of the time variable: The derivative u' is approximated by the simple forward difference

$$u' = \frac{\partial u}{\partial t} \approx \frac{u(t + \Delta t) - u(t)}{\Delta t}. \quad (37)$$

Substituting Eq. (37) into Eq. (36) gives

$$\frac{\partial E(u)}{\partial u_i} \approx \sum_{e \in D} \left\{ [A]^e \{u(t + \Delta t)\}^e + [P]^e \left\{ \frac{u(t + \Delta t) - u(t)}{\Delta t} \right\}^e - \{q^*\}^e \right\} = \sum_{e \in D} \left\{ \left\{ [A]^e + \frac{1}{\Delta t} [P]^e \right\} \{u(t + \Delta t)\}^e - \frac{1}{\Delta t} [P]^e \{u(t)\}^e - \{q^*\}^e \right\}. \quad (38)$$

7. Because the condition for an extremum of the function $E(u)$ is $\frac{\partial E(u)}{\partial u_i} = 0$, Eq. (38) can be expressed as the linear system

$$\sum_{e \in D} \left\{ [A]^e + \frac{1}{\Delta t} [P]^e \right\} \{u(t + \Delta t)\}^e = \sum_{e \in D} \left\{ \frac{1}{\Delta t} [P]^e \{u(t)\}^e - \{q^*\}^e \right\}. \quad (39)$$

8. Because the functional matrix $\{[A]^e + \frac{1}{\Delta t} [P]^e\}$ in Eq. (39) is positive definite and symmetric, Eq. (39) is a system of m equations for the m values of u_i at the inner nodes. Therefore, when $u(x, y, 0) = u_0(x, y)$ is set as an initial value, the water head values for every inner node at $t = \Delta t$ can be computed.

9. In the same way, the m_l values at the external nodes on the impermeable boundary are given by m_l equations that are similar to Eq. (39). Based on the initial value condition, the water head values for every external node can be calculated too.

Based on the laboratory results for the initial values of the parameters (Table 7), we can simulate the space–time distribution of the flow for the T_{2l}^1 reservoir (Table 8 and Fig. 10).

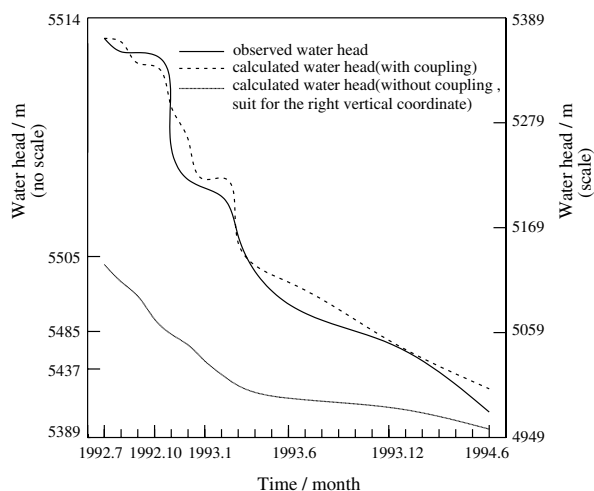
As anticipated, including the effects of temperature and pressure improves the simulation results, in particular, the time–space distribution of water head. Table 8 compares the simulation results for the water head from the calculations with the measured values. Results from the model including the temperature and pressure effects are much closer to, but slightly larger than measured values (Fig. 10). The reason for the overprediction may be the decrease of water's percolation parameters with higher

Table 7 Test result of seepage parameters' initial values of T_{2l}^1 reservoir in Moxi structure (temperature = 50 °C)

Kind of area	k_0 ($\times 10^{-3} \mu\text{m}^2$)	n_0 (%)	β_{s0} ($1 \text{ MPa} \times 10^{-4}$)	β_{w0} ($1 \text{ MPa} \times 10^{-4}$)	ν_0 (P)
Abundant water part I	0.234	6.360	2.174	2.865	1.170
Moderate abundant water part II	0.164	4.452	1.522	2.865	1.170
Poor water part III	0.117	3.180	1.087	2.865	1.170

Table 8 Comparison of water head calculated by FEM and actual water head

Time	Well number	Actual water head (m)	With coupling		Without coupling	
			Calculated water head (m)	Imitation error (%)	Calculated water head (m)	Imitation error (%)
October 1992	10	5437.940	5493.931	1.03	4890.339	-10.07
	14	5505.967	5512.383	0.12	5052.826	-8.23
	53	5512.396	5512.804	0.00	5073.058	-7.97
	58	5510.843	5513.690	0.05	5068.873	-8.02
	80	5509.679	5514.247	0.08	4982.954	-9.56
	100	5508.235	5514.801	0.12	5000.927	-9.21
	108	5508.291	5512.600	0.08	5013.646	-8.98
	114	5486.680	5514.428	0.51	5049.940	-7.96

**Figure 10** Observed water head line and calculated water head line of No. 53 well in Moxi structure.

pressure and temperature; this can contribute to the water's pore pressure increment. Thus, neglecting the effect of higher pressure and temperature on the migration of deeply buried water can lead to the greater simulation error. Here we should note that in this case we consider the effect of the higher temperature through the following two aspects: (1) taking account of the water's viscosity variation with temperature; and (2) taking account of the other initial coefficients' values at temperature reaching 50 °C.

Conclusions

In the present study, we developed a revised model by simply describing the deeply buried groundwater migration under coupled hydraulic, thermal and mechanical processes.

The following conclusions can be drawn from the model development and numerical simulation results:

- The migration of groundwater in deeply buried aquifers is strongly affected by the higher pressure and temperature conditions that exist there, especially by the higher pressure conditions.
- Generally these effects can be included in the variation of seepage parameters such as hydraulic conductivity K and storage coefficient S , which can, in turn, be expressed in terms of solid skeleton's permeability k , porosity n , compressibility coefficient β_s , seepage fluid's viscosity μ , and compressibility coefficient β_w . That is to say, through these parameters' variation with pressure or temperature change, the effects have been quantitatively represented.
- The result of the laboratory tests indicates that all of the above parameters' variation can be represented by negative exponential functions.
- Based on mathematical transformation and some linear methods, we show that the revised model has the same form as the standard one for shallow groundwater flow. In particular, the effects of the higher pressure are included in the function variable u , and in its revised parameters such as K_x^* , K_y^* , Q^* , S^* . More importantly, these transformations make it possible to use existing calculation programs for the new model. This is not only more convenient but also avoids errors due to reprogramming. The example application shows that this revised model is successful. Comparing the water head simulation result, we can find that the results including the effects of higher temperature and pressure agree better with observed values than the calculations that neglect these effects. This also confirms that the effects of higher pressure and temperature should be included in studies of deeply buried groundwater migration.

Finally, the coupled thermo-hydro-mechanical (THM) process is relatively complicated. In this paper, the complete coupling has been simplified. More generally, it may be necessary to include phase changes of the fluid under high temperature (such as evaporation and thus induced vapour flow and heat convection), which have been neglected here. A full treatment of the coupled THM system requires the three governing equations of mass conservation, momentum conservation and energy conservation and their coupling mechanisms. In this paper, we have considered only the mass and momentum conservation equations, but we have included indirect parametric coupling for effects of temperature and stress on parameters (see Eqs. (1) and (30)). The equation of energy conservation has not been used and, as a result, the evolution of temperature in the FEM model cannot be properly simulated. Therefore, the effects of temperature can only be considered by assuming specific (and uniformly distributed) temperature and its effects on other mechanical/seepage parameters. So the THM processes' simulation considered in this paper is a simplification of the fully coupled problem which we intend to address in future research.

Acknowledgments

The author thank Professor A. Packman of Northwestern University for his advice on this work and his support during author's visit to Northwestern University. The author is also grateful to Dr. He YL for his laboratory test and analysis work. The research presented here has been supported by the National Natural Science Foundation of China through Grant No. 40302033, and also by the Chinese Scholarship Council through Grant No. 21851038.

References

- Academic Institute of Hydrogeological and Engineering Geology of Chinese Geological Ministry, 1982. *Generation of Deep Buried Brine and its Research Method*. Geological Press, Beijing.
- Asadi, M., Ghalambor, A., Shirazi, M.K., 1997. Assessment of jet perforated rock damage by finite element method. Paper SPE Presented at European Formation Damage Control Conference. Society of Petroleum Engineers, Hague, The Netherlands, pp. 25–32.
- Asadi, M., Shirazi, M.K., Ghalambor, A., Pratt, D.W., 2001. Experimental and simulation analysis of jet-perforated rock damage. *SPE Drilling and Completion* 16 (3), 176–181.
- Bear, J., 1988. *Dynamics of Fluids in Porous Media*. Dover, New York, p. 764.
- Borja, R.I., 1992. Free-boundary, fluid flow, and seepage force in excavations. *Journal of Geotechnical Engineering – ASCE* 118 (1), 125–146.
- Budhu, M., Gobin, R., 1995. Seepage-induced slope failures on sandbars in Grand Canyon. *Journal of Geotechnical Engineering – ASCE* 121 (8), 601–609.
- Chardac, O., Brie, A., Chouker, A.C., 2003. Correlations of shear vs. compressional in Shaly sands and application to quicklook hydrocarbon detection. Paper SPE Presented at SPE Annual Technical Conference and Exhibition. Society of Petroleum Engineers, Denver, CO, USA, pp. 1347–1355.
- Chen, M.Y., 1993. *Calculative Program for Seepage*. China University of Geosciences, Beijing, pp. 2–16.
- Corfdir, A., 2004. Limit analysis for saturated porous media without fluid flow calculation. *International Journal for Numerical and Analytical Methods in Geomechanics* 28 (6), 543–561.
- Ehlig-Economides, C.A., Economides, M.J., 2002. Recipe for success in ultradeep water. Paper SPE Presented at SPE Annual Technical Conference and Exhibition. Society of Petroleum Engineers, San Antonio, TX, USA, pp. 2481–2493.
- Fernandez, G., Alvarez, T.A., 1994. Seepage-induced effective stresses and water pressures around pressure tunnels. *Journal of Geotechnical Engineering – ASCE* 120 (1), 108–128.
- Fisher, Q.J., Casey, M., Harris, S.D., Knipe, R.J., 2003. Fluid-flow properties of faults in sandstone: the importance of temperature history. *Geology* 31 (11), 965–968.
- Fung, L.S.K., Wong, R.C.K., 1996. Modelling of cavity stability and sand production in heavy oil reservoirs. *Journal of Canadian Petroleum Technology* 35 (2), 47–52.
- Ge, J.L., 1982. *Seepage Mechanics in Petroleum and Oil Reservoir*. Petroleum Industry Press, Beijing.
- Hart, R.D., John, C.M.S.T., 1986. Formulation of a fully-coupled thermal–mechanical–fluid flow model for non-linear geologic systems. *International Journal of Rock Mechanics and Mining Science & Geomechanics Abstracts* 23 (3), 213–224.
- Holder, J., Thallak, S., Yunus, J., Gray, K.E., 1993. Modulus and permeability variations during air/water flow in Shaley sandstones. *International Journal of Rock Mechanics and Mining Sciences & Geomechanics Abstracts* 30 (7), 771–777.
- Hsi, J.P., Small, J.C., 1992. Ground settlements and drawdown of the water-table around an excavation. *Canadian Geotechnical Journal* 29 (5), 740–756.
- Huang, T., 1996. Study of deep buried brine seepage mathematical model under abnormal temperature and pressure conditions. *Hydrogeology and Engineering Geology* (1), 35–39.
- Jing, L., Tsang, C.-F., Stephansson, O., 1995. DECOVALEX – an international co-operative research project on mathematical models of coupled T-H-M processes for safety analysis of radioactive waste repositories. *International Journal of Rock Mechanics and Mining Sciences & Geomechanics Abstracts* 32 (5), 389–398.
- Jouanna, P., Montiel, A., Duruisseaud, P., 1998. Importance of stress on percolation in fissured superficial rock. *Experimental evidence*. *Bulletin de la Societe Geologique de France* 169 (6), 753–763.
- Khaksar, A., Griffiths, C.M., McCann, C., 1999. Compressional- and shear-wave velocities as a function of confining stress in dry sandstones. *Geophysical Prospecting* 47 (4), 487–508.
- Kok, M.V., Gurkan Iscan, A., Buket Ulker, E., 2002. Effect of axial stresses on reservoir rocks. *Energy Sources* 24 (10), 915–920.
- Lander, R.H., Walderhaug, O., 1999. Predicting porosity through simulating sandstone compaction and quartz cementation. *AAPG Bulletin (American Association of Petroleum Geologists)* 83 (3), 433–449.
- Li, G.C., Desai, C.S., 1983. Stress and seepage analysis of earth dams. *Journal of Geotechnical Engineering – ASCE* 109 (7), 946–960.
- Li, S.P., Li, Y.S., Li, Y., Wu, Z.Y., Gang, Z., 1994. Permeability–strain equations corresponding to the complete stress–strain path of Yin Zhuang sandstone. *International Journal of Rock Mechanics and Mining Sciences & Geomechanics Abstracts* 31 (4), 383–391.
- Lindborg, U., 2002. Fatigue-induced shape change in marble. Paper MMS Presented at Mechanisms and Mechanics of Fracture: The John Knott Symposium. Minerals, Metals and Materials Society, Columbus, OH, USA, pp. 269–274.
- Liu, J., Ng, C.W.W., 2003. Numerical studies on the influence of stress-state and wetting path on transient seepage in saturated–unsaturated soils. *Eurasian Soil Science* 36 (1), 71–75.
- Menendez, B., David, C., Nistal, A.M., 2001. Confocal scanning laser microscopy applied to the study of pore and crack networks in rocks. *Computers and Geosciences* 27 (9), 1101–1109.

- Morita, N., Gray, K.E., 1992. Rock-property changes during reservoir compaction. *SPE Formation Evaluation* 7 (3), 197–205.
- Palciauskas, V.V., Domenico, P.A., 1982. Characterization of drained and undrained response of thermally loaded repository rocks. *Water Resources Research* 18 (2), 281–290.
- Reid, M.E., Iverson, R.M., 1992. Gravity-driven groundwater-flow and slope failure potential. 2. Effects of slope morphology, material properties, and hydraulic heterogeneity. *Water Resources Research* 28 (3), 939–950.
- Rinaldi, M., Casagli, N., Dapporto, S., Cargini, A., 2004. Monitoring and modelling of pore water pressure changes and riverbank stability during flow events. *Earth Surface Processes and Landforms* 29 (2), 237–254.
- Rutqvist, J., Borgesson, L., Chijimatsu, M., Kobayashi, A., Jing, L., Nguyen, T.S., Noorishad, J., Tsang, C.-F., 2001. Thermohydromechanics of partially saturated geological media: governing equations and formulation of four finite element models. *International Journal of Rock Mechanics and Mining Science* 38 (1), 105–127.
- Rutter, E.H., Hadizadeh, J., 1991. On the influence of porosity on the low-temperature brittle–ductile transition in siliciclastic rocks. *Journal of Structural Geology* 13 (5), 609–614.
- Shen, Z.L., 1985. *Hydrogeology*. Academic Press, Beijing.
- Simon, A., Collison, A.J.C., 2001. Pore-water pressure effects on the detachment of cohesive streambeds: seepage forces and matric suction. *Earth Surface Processes and Landforms* 26 (13), 1421–1442.
- Skomedal, E., Jostad, H.P., Hettrema, M.H., 2002. Effect of pore pressure and stress path on rock mechanical properties for HPHT application. Paper SPE Presented at SPE/ISRM Rock Mechanics in Petroleum Engineering Conference. Society of Petroleum Engineers, Irving, TX, USA, pp. 36–45.
- Sridharan, A., Prakash, K., 2001. Consolidation and permeability behavior of segregated and homogeneous sediments. *Geotechnical Testing Journal* 24 (1), 109–120.
- Tomlinson, S.S., Vaid, Y.P., 2000. Seepage forces and confining pressure effects on piping erosion. *Canadian Geotechnical Journal* 37 (1), 1–13.
- Xue, Y.Q., Xie, C.H., 1980. *Numerical Methods in Hydrogeology*. Coal Industry Press, Beijing.
- Yang, L.Z., 1990. Research development of deeply buried groundwater in foreign lands and domestic situation in this field. *Chinese Geology* (12).
- Yang, L.Z., 1995. *Study of Deeply Buried Groundwater's Seepage*. Chengdu Science and Technology University Press, Chengdu.
- Zeng, Z.W., Grigg, R., Ganda, S., 2003. Experimental study of overburden and stress influence on non-Darcy gas flow in Dakota sandstone. Paper SPE Presented at SPE Annual Technical Conference and Exhibition. Society of Petroleum Engineers, Denver, CO, USA, pp. 377–386.
- Zhao, Y.S., Yang, D., Zheng, S.H., Hu, Y.Q., 1999. Experimental study on water seepage constitutive law of fracture in rock under 3D stress. *Science in China Series E – Technological Sciences* 42 (1), 108–112.